Mon. Not. R. Astron. Soc. **000**, 1–26 (2015) Printed 14 August 2015 (MN LaTeX style file v2.2)

A spiral galaxy's mass distribution uncovered through lensing and dynamics

W. Trick[1]*, G. van de Ven[1] and A. Dutton[1]
[1] *Max-Planck-Institute for Astronomy, Königstuhl 17, 69117 Heidelberg, Germany*

Accepted ????. Received ????; in original form ????

ABSTRACT

We analyse the stellar and dark matter distribution in the spiral galaxy SDSS J1331+3638 (J1331) by means of two independent methods: gravitational lensing and dynamical Jeans modelling. Hubble Space Telescope (HST) imaging by Treu et al. (2011) reveals, that J1331's bulge is superimposed by a quadruplet of extended lensing images. By fitting a gravitational potential model to the image positions, we constrain the mass inside the Einstein radius ($R_{\mathrm{ein}} = 0.91 \pm 0.02$ arcsec) to within 4% ($M_{\mathrm{ein}} = (7.8 \pm 0.3) \cdot 10^{10} M_{\odot}$). From Multi-Gaussian Expansions (MGE) of J1331's surface brightness distribution we find that J1331 has a total luminosity of $L_{I,tot} \simeq 5.6 \cdot 10^{10} L_{I,\odot}$ and an effective radius of $R_{\mathrm{eff}} \simeq 2.6$ arcsec = 5.6 kpc. [TO DO: apparent brightness is boring, right?]

According to the long-slit major axis stellar kinematics from Dutton et al. (2013), J1331 has a counter-rotating stellar core inside ~ 2 arcsec. We model the observed stellar kinematics in J1331's central regions by finding MGE models for the stellar and dark matter distribution that solve the axisymmetric Jeans equations. We find that J1331 requires a steep total mass-to-light ratio gradient in the center to reproduce the observed stellar kinematics. The best fit dynamical model predicts a total mass inside the Einstein radius consistent with the lens model, and vice versa the lens model gives an successful prediction for the observed kinematics in the galaxy center. For a dynamical model including a NFW dark matter halo, we constrain the halo to have virial velocity $v_{200} \simeq 240 \pm 40$ km/s and a concentration of $c_{200} \simeq 8 \pm 2$ in case of a moderate tangential velocity anisotropy of $\beta_z \simeq 0.4 \pm 0.1$. The NFW halo models can successfully reproduce the signatures of J1331's counter-rotating stellar core and predict J1331's rotation curve at larger radii. However, all these models were more massive than expected from the gas rotation curve at larger radii, and failed to reproduce the steep drop in measured velocity dispersion at [TO DO: WHAT RADIUS???]. This could indicate a non-trivial re-distribution of matter due a possible minor merger event in J1331's past.

Key words: blabla – blabla: bla.

* E-mail: trick@mpia.de

1 INTRODUCTION

[TO DO]

Dark matter general

- The flat rotation curves of galaxies were the first indication, that galaxies could reside in large and massive, more or less spherical halos made of invisible dark matter $\longrightarrow$ stellar movements in solar neighbourhood (Oort 1932), $H\alpha$ rotation curves of external galaxies (Rubin et al. 1978)
- Standard model of cosmology, based on the by the Planck Mission, predicts $\sim$ 32% of the universes content is in the form of matter and $\sim$ 85% of the total matter is non-baryonic dark matter.

Lensing to measure mass

- Completely independent method to measure mass of galaxies is gravitational lensing
- massive galaxies can act as gravitational lenses, deflect light of background sources, gives rise to multiple images
- By 2010 over 200 strong gravitational galaxy lenses had been discovered (Treu 2010) and the number is still rising
- On galaxy scales strong gravitational lensing is sensitive to the total projected matter amount inside approximately $\sim$ 1 arcsec.

Dynamical modelling to measure mass

- Gas rotation curves are useful to measure matter distribution at large radii
- gas on circular orbits $\longrightarrow$ directly circular velocity curve and mass profile.
- But: gas has dissipative nature, concentrated to midplane $\longrightarrow$ sensitive to disturbances by e.g. bars, spiral arms
- stars are dissipationless, present almost everywhere in the galaxy $\longrightarrow$ very good tracers of the underlying gravitational potential $\longrightarrow$ but much more complex motions: bulk rotation around principal axis, plus random motion components in all coordinate directions $\longrightarrow$ velocity anisotropy $\longrightarrow$ degeneracy with matter distribution
- modelling: account for stellar rotation, dispersion and velocity anisotropy
- e.g. solution of the Jeans equations for an assumed velocity anisotropy, e.g. Cappellari (2008)
- dynamical modelling of stellar kinematics also at smaller radii $\longrightarrow$ complement lensing investigation of the matter distribution in the center of galaxies
- Other modelling methods: Schwarzschild's orbital superposition approach (van den Bosch et al. 2008)

Dark Matter Halos

- Cosmological cold dark matter N-body simulations suggest that dark matter halos take a cuspy shape, following a NFW profile (Navarro et al. 1996)
- central dark matter density cusps are not observed in dark matter dominated galaxies (dwarfs); if they exist in more massive galaxies depends strongly on stellar mass-to-light ratio. Overall, observations suggest cored dark matter halos $\longrightarrow$ core-cusp problem, might be due to a yet unknown interaction between dark matter and baryons

SWELLS Survey

TO DO

Characteristics of J1331

- SDSS J1331+3638 (J1331)
- approximate hubble type Sb
- first discovered by Sloan digital sky survey (SDSS) [TO DO: REF]
- at redshift $z_d \simeq 0.113$ [TO DO: REF]
- Treu et al. (2011) identified it as a strong lens
- large reddish bulge and bluish spiral arms, see Fig. 1a and 1b
- superimposed by quadruplet of extended bluish images at a redshift of $z_s \simeq 0.254$ [TO DO: REF], see Fig. 1c
- lensed object might be a star-forming blob of a background galaxy.
- Lensing properties first analysed by Brewer et al. (2012)
- rather edge-on $\longrightarrow$ possible to measure rotation curves. Dutton et al. (2013) measured the gas and stellar rotation curves along the major axis. Fitted galaxy model to gas kinematics at large radii, and lensing result
- large counter-rotating core, see Fig. 1d
- possible minor merger in the past

Goal of this work

- constraining the matter distribution in a galaxy, disentangling stellar and dark matter component at smaller radii
- using two independent methods, lensing and dynamics
- testing, if Jeans modelling works also in the presence of counter-rotating cores
- focus on the smaller radii, as Dutton et al. (2013) was focusing on outer regions
- complementing the work by [SWELLS paper on lensing and lensing/dynamcis TO DO: find] by an in depth analysis
- ideal case: investigating how a minor merger modifies the mass distribution of a galaxy

Data used

- Hubble Space Telescope (HST)/WFPC2/WFC3 imaging by Treu et al. (2011), see Fig. 1a and 1b
- Dutton et al. (2013) measured the gas and stellar rotation curves along the major axis. see Fig. 1b and 1d

Methods

- similar analysis of J1331 as van de Ven et al. (2010) has done with the Einstein cross
- lensing: fitting scale-free galaxy model to image positions (Evans & Witt 2003)
- photometry: MGE expansion of surface brightness in the F814W filter (deconvolution with PSF), apparent magnitude, total luminosity, effective radius
- Jeans modelling: jeans axisymmetric modelling (JAM) by Cappellari (2008) to fit model predictions for the second velocity moments to the stellar kinematics data

[TO DO]

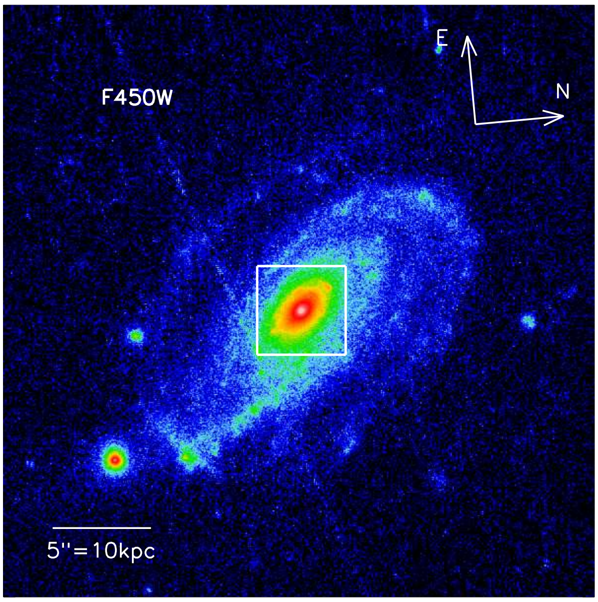

(a) J1331 in F450W ("blue")

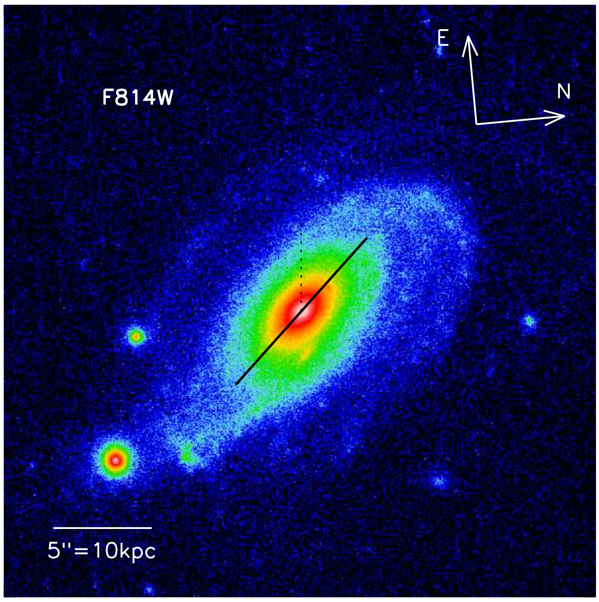

(b) J1331 in F814W ("red")

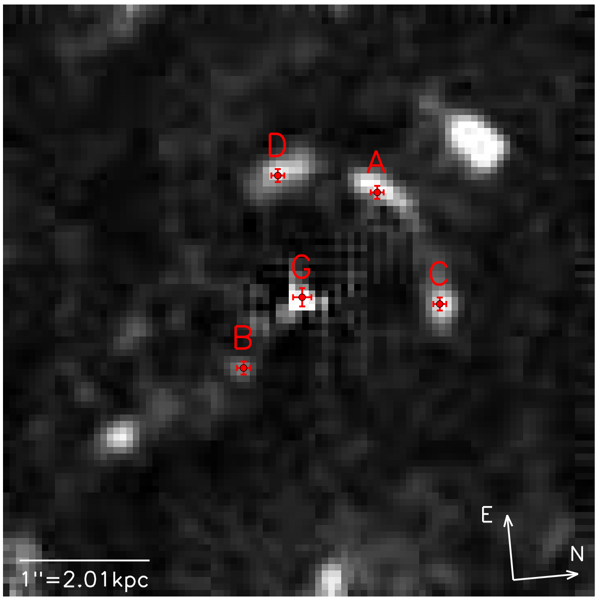

(c) The lensing images

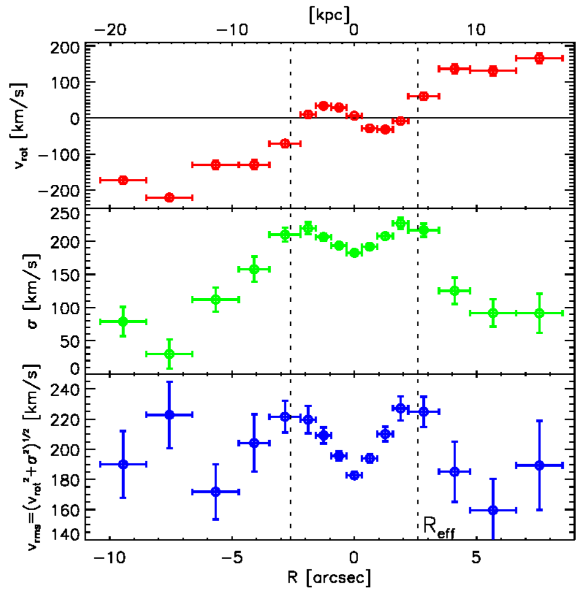

(d) Stellar Kinematics by Dutton et al. (2013)

Figure 1. Hubble Space telescope (HST) images and stellar kinematics of the galaxy SDSS J1331+3638 (J1331), which has a large counter-rotating core and whose bulge acts as a strong lens for a bluish background source. *Panel (a) and (b):* HST/WFPC2/WFC3 images of J1331 by Treu et al. (2011) in two filters, F450W in panel (a) and F814W in panel (b). The galaxy's coordinates on the sky are right ascension $\alpha = 202.91800°$ and declination $\delta = 36.46999°$ (epoch J2000). Image orientation and scaling are indicated in panel (a); the scaling transformation from arcseconds to the physical size of the galaxy in kpc uses the galaxy's redshift $z_d = 0.113$ (Brewer et al. 2012) (i.e. assumes an angular diameter distance of 414 Mpc). The color scaling of these two images is the same. The black solid line in panel (b) shows the orientation of the major-axis. The line has a length of 10 arcsec and indicates the region within which we carry out the Jeans modelling. [TO DO: NOT ALL THE TIME.???????] *Panel (c):* The central region of J1331 in F450W, surface brightness subtracted. An IRAF ellipse ???? fit to the F450W surface brightness in panel (a) was subtracted from the image. The (smoothed) residuals within the white square in panel (a) are shown in panel (c). Four bright blobs (A,B,C and D) become visible, which are arranged in a typical strong lensing configuration around the center of the galaxy (G). *Panel (d):* Stellar Kinematics along the galaxy's major axis as measured by Dutton et al. (2013), line-of-sight rotation velocity $v_{\rm rot}$, line-of-sight velocity dispersion σ and the rms-velocity $v_{\rm rms} = \sqrt{v_{\rm rot}^2 + \sigma^2}$. The dotted line in panel (b) indicates the galaxy's effective half-light radius (in the F814W filter), $R_{\rm eff} = 2.6" = 5.2$ kpc. The $v_{\rm rot}$ curve reveals that J1331 is counter-rotating within $R_{\rm eff}$. [TO DO: Add (x,y) axis in figure b).???????]

2 MODELLING

2.1 Multi-Gaussian Expansion Formalism

Multi-Gaussian Expansions (MGE) are used to parametrize the observed surface brightness or projected total mass of a galaxy as a sum of N two-dimensional, elliptical Gaussians (Bendinelli 1991; Monnet et al. 1992; Emsellem et al. 1994, 1999). This work makes use of the algorithm and code[1] by Cappellari (2002). We assume all Gaussians to have the same center and position angle ϕ, i.e. orientation of w.r.t. the y'-axis of the coordinate system with polar coordinates (R', θ') [TO DO: CHECK]. Then the surface brightness can be written as

$$\begin{aligned} I(R',\theta') &= \sum_{i=1}^{N} I_{0,i} \exp\left[-\frac{1}{2\sigma_i^2}\left(x'^2 + \frac{y'^2}{q_i'^2}\right)\right] && (1)\\ \text{with } I_{0,i} &= \frac{L_i}{2\pi\sigma_i^2 q_i'} && (2)\\ \text{and } x_i' &= R'\cos(\theta'-\phi)\\ y_i' &= R'\sin(\theta'-\phi), \end{aligned}$$

where $I_{0,i}$ is the central surface brightness of each Gaussian, L_i its total luminosity, σ_i its dispersion along the major axis and q_i' the axis ratio between the elliptical Gaussians major and minor axis.
We can also expand the telescopes point-spread function (PSF) as a sum of circular Gaussians,

$$\mathrm{PSF}(x,y) = \sum_j \frac{G_j}{2\pi\delta_j^2} \exp\left[-\frac{1}{2\delta_j^2}\left(x^2+y^2\right)\right], \qquad (3)$$

where $\sum_j G_j = 1$ and δ_j are in this case the dispersions of the circular PSF Gaussians. In this case the observed surface brightness distribution is a convolution of the intrinsic surface brightness in Eq. (1) with the PSF in Eq. (3): $(I * \mathrm{PSF})(x', y')$ is then again a sum of Gaussians and can be directly fitted to an image of the galaxy in question.

$I(R', \theta')$ describes the intrinsic, to 2D projected light distribution or surface density of the galaxy. Under the assumption that the galaxy is oblate and axisymmetric, and given the inclination angle i of the galaxy with respect to the observer, MGEs allow an analytic deprojection of the 2D MGE to get a 3D light distribution or density $\nu(R, z)$ for the galaxy,

$$\nu(R,z) = \sum_i \nu_{0,i} \exp\left[-\frac{1}{2\sigma_i}\left(R^2 + \frac{z^2}{q_i^2}\right)\right]. \qquad (4)$$

The flattening of each axisymmetric 3D Gaussian q and its central density $\nu_{0,i}$ follow from the observed 2D axis ratio q_i' and surface density $I_{0,i}$ as

$$\begin{aligned} q_i^2 &= \frac{q_i'^2 - \cos^2 i}{\sin^2 i}\\ \nu_{0,i} &= \frac{q_i' I_{0,i}}{q_i\sqrt{2\pi\sigma_i^2}}. \end{aligned}$$

[1] Michele Cappellari's IDL code package for fitting MGEs to images is available online at `http://www-astro.physics.ox.ac.uk/~mxc/software`. The version from June 2012 was used in this work.

2.2 Strong Gravitational Lensing Formalism and Lens Model

Lensing Formalism. A gravitational lens is a mass distribution, whose gravitational potential Φ acts as a lens for light coming from a source positioned somewhere on a plane behind the lens. The angular diameter distance from the observer to the lens is D_d, to the source plane it is D_s and the distance between the lens and source plane is D_{ds}. The deflection potential of the lens is its potential, projected along the line of sight z and rescaled to

$$\psi(\vec{\theta}) := \frac{D_{ds}}{D_d D_s}\frac{2}{c^2}\int \Phi(\vec{r} = D_d\vec{\theta}, z)\, \mathrm{d}z, \tag{5}$$

where $\vec{\theta}$ is a 2-dimensional vector on the plane of the sky. The light from the source at $\vec{\beta} = (\xi, \eta)$ is deflected according to the lens equation

$$\vec{\beta} = \vec{\theta}_i - \vec{\nabla}_\theta \psi(\vec{\theta})\Big|_{\vec{\theta}_i} \tag{6}$$

into an image $\vec{\theta}_i = (x_i, y_i)$. The gradient of the deflection potential $\vec{\nabla}_\theta\psi(\vec{\theta})$ is equal to the angle by which the light is deflected multiplied by D_{ds}/D_s.

The total time delay of an deflected light path through $\vec{\theta}$ with respect to the unperturbed light path is given by

$$\Delta t(\vec{\theta}) = \frac{(1+z_d)}{c}\frac{D_d D_s}{D_{ds}}\left[\frac{1}{2}(\vec{\theta} - \vec{\beta})^2 - \psi(\vec{\theta})\right], \tag{7}$$

(Narayan & Bartelmann 1999). According to Fermat's principle the image positions will be observed at the extrema of $\Delta t(\vec{\theta})$.

The inverse magnification tensor

$$\mathscr{M}^{-1} \equiv \frac{\partial\vec{\beta}}{\partial\vec{\theta}} \overset{(6)}{=} \left(\delta_{ij} - \frac{\partial^2\psi}{\partial\theta_i\partial\theta_j}\right) \tag{8}$$

describes how the source position changes with image position. It also describes the distortion of the image shape for an extended source and its magnification due to lensing according to

$$\mu \equiv \frac{\text{image area}}{\text{source area}} = \det\mathscr{M}.$$

Lines in the image plane for which the magnification becomes infinite, i.e. $\det\mathscr{M}^{-1} = 0$, are called *critical curves.* The corresponding lines in the source plane are called *caustics.* The position of the source with respect to the caustic detemines the number of images and their configuration and shape with respect to each other.

The *Einstein mass* M_{ein} and *Einstein radius* R_{ein} are defined via the relation

$$M_{\text{ein}} \equiv M_{\text{proj}}(< R_{\text{ein}}) \overset{!}{=} \pi\Sigma_{\text{crit}}R_{\text{ein}}^2,$$

where $\Sigma_{\text{crit}} \equiv \frac{c^2}{4\pi G}\frac{D_s}{D_d D_{ds}}$ is the critical density and $M_{\text{proj}}(< R_{\text{ein}})$ is the mass projected along the line-of-sight within R_{ein}. M_{ein} is similar to the projected mass within the critical curve M_{crit}.

Lens Model. Following Evans & Witt (2003) we assume a scale-free model

$$\psi(R', \theta) = R'^{\alpha}F(\theta)$$

for the lensing potential, consisting of an angular part $F(\theta)$ and a power-law radial part, with (R', θ) being polar coordinates on the plane of the sky. The case $\alpha = 1$ corresponds to a flat rotation curve. We expand $F(\theta)$ into a Fourier series,

$$F(\theta) = \frac{a_0}{2} + \sum_{k=1}^{\infty}\left(a_k\cos(k\theta) + b_k\sin(k\theta)\right). \tag{9}$$

For this scale-free lens model the lens equation (6) becomes

$$\begin{pmatrix}\xi\\ \eta\end{pmatrix} = \begin{pmatrix} R'_i\cos\theta_i - R_i'^{\alpha-1}\left(\alpha\cos\theta_i F(\theta_i) - \sin\theta_i F'(\theta_i)\right)\\ R'_i\sin\theta_i - R_i'^{\alpha-1}\left(\alpha\sin\theta_i F(\theta_i + \cos\theta_i F'(\theta_i)\right)\end{pmatrix} \tag{10}$$

(Evans & Witt 2003), where $F'(\theta) = \partial F(\theta)/\partial\theta$. When we fix the slope α, then the lens equation is a purely linear problem and can be solved numerically for the source position (ξ, η) and the Fourier parameters (a_k, b_k) given one observed image at position $(x_i = R'_i\cos\theta_i, y_i = R'_i\sin\theta_i)$.

Model fitting. As described above our lensing model has the following free parameters: the source position (ξ, η), and the radial slope α and Fourier parameters (a_k, b_k) of the lens mass distribution in eq. (2.2) and (9). We want to find the lensing model which minimizes for all four images the distance between the observed image positions $\vec{\theta}_{oi}$ and those predicted by the lensing model $\vec{\theta}_{pi}$. Because we want to avoid solving the lens equation (cf. eq. (6) and (10)) for θ_{pi}, we follow Kochanek (1991) and cast the calculation back to the source plane using the magnification tensor in eq. (8):

$$\begin{aligned}\chi^2_{\text{lens}} &= \sum_{i=1}^{4}\left|\begin{pmatrix}\frac{1}{\Delta_x} & 0\\ 0 & \frac{1}{\Delta_y}\end{pmatrix}\left(\vec{\theta}_{pi} - \vec{\theta}_{oi}\right)\right|^2\\ &\simeq \sum_{i=1}^{N}\left|\begin{pmatrix}\frac{1}{\Delta_x} & 0\\ 0 & \frac{1}{\Delta_y}\end{pmatrix}\mathscr{M}|_{\vec{\theta}=\vec{\theta}_{oi}}\begin{pmatrix}\xi - \tilde{\xi}_i\\ \eta - \tilde{\eta}_i\end{pmatrix}\right|^2,\end{aligned}$$

where (Δ_x, Δ_y) are the measurement errors of the image positions $\vec{\theta}_{oi}$. $\mathscr{M}|_{\vec{\theta}=\vec{\theta}_{oi}}$ is the magnification tensor and $(\tilde{\xi}_i, \tilde{\eta}_i)$ the source position according to the lens equation evaluated at $\vec{\theta}_{oi}$. Following van de Ven et al. (2010) we add a term

$$\chi^2_{\text{shape}} = \lambda\sum_{k\geqslant 3}\frac{\left(a_k^2 + b_k^2\right)}{a_0^2}$$

which forces the shape of the mass distribution to be close to an ellipse. The total χ^2 to minimize is therefore

$$\chi^2 = \chi^2_{\text{lens}} + \chi^2_{\text{shape}}$$

We set $a_1 = b_1 = 0$, which corresponds to the choice of origin; in this case the center of the galaxy.

To be able to constrain the slope α, we would have needed flux ratios for the images as in van de Ven et al. (2010). But the extended quality of the images and the uncertainty in surface brightness subtraction makes flux determination too unreliable and we do not include them in the fitting. Even though the constraint from just the image position fit on α is very weak, we were however able to show that the image positions in tab. 4 minimize χ^2 at $\alpha = 1$ and also our other image position sets from different models and filters are consistent with a flat rotation curve. In the following we therefore set $\alpha = 1$.

2.3 Jeans Axisymmetric Modelling (JAM)

Jeans axisymmetric models (JAM) assume galaxies (a) to be collisionless, i.e. the collisionless Boltzmann equation for the distribution function $f(\boldsymbol{x}, \boldsymbol{v}, t)$ has to be satisfied ($\frac{\mathrm{d}f(\boldsymbol{x},\boldsymbol{v},t}{\mathrm{d}t} = 0$), (b) in a steady state ($\frac{\partial}{\partial t} = 0$), (c) axisymmetric (best described in cylindrical coordinates (R, z, ϕ) and $\frac{\partial}{\partial \phi} = 0$). From this follow the axisymmetric Jeans equations as the vector-valued first moment of the Boltzmann equation, i.e.

$$\int \frac{\mathrm{d}f}{\mathrm{d}t}\,\mathrm{d}^3 v = 0.$$

To be able to solve the Jeans equations, additional assumptions about the velocity ellipsoid tensor $\langle v_i v_j \rangle$ have to be made. We follow Cappellari (2008) and assume firstly, that the galaxy's velocity ellipsoid is aligned with the cylindrical coordinate system, i.e. $\langle v_i v_j \rangle = 0$ for $i \neq j$. Secondly, we assume a constant ratio between the radial and vertical 2nd velocity moments, $\beta_z \equiv 1 - \langle v_z^2 \rangle / \langle v_R^2 \rangle$. This reduces the Jeans equations to two equations for $\langle v_z^2 \rangle$ and $\langle v_\phi^2 \rangle$, that can be solved by means of one integration,

$$\begin{aligned} n\langle v_z^2 \rangle(R,z) &= \int_0^\infty n \frac{\partial \Phi}{\partial z}\,\mathrm{d}z \\ n\langle v_\phi^2 \rangle(R,z) &= R\frac{\partial}{\partial R}\left(\frac{n\langle v_z^2\rangle}{1-\beta_z}\right) + \frac{n\langle v_z^2\rangle}{1-\beta_z} + Rn\frac{\partial \Phi}{\partial R}, \end{aligned}$$

where $n(\boldsymbol{x}) = \int f(\boldsymbol{x}, \boldsymbol{v})\,\mathrm{d}3v$ is the number density of tracers and $\Phi(\boldsymbol{x})$ the galaxy's gravitational potential, generated by the mass density $\rho(\boldsymbol{x})$ via Poisson's equation.

The JAM modelling approach by Cappellari (2008) makes use of expressing the tracer density and the mass density as MGEs (see also [TO DO: REF: Emsellem et al. 19994]). The density of stellar tracers is assumed to be proportional to the observed and deprojected brightness distribution $\nu(R, z)$ in Eq. (4). The mass density consists of several sets of MGEs: One MGE, that is usually taken to be $\nu(R, z)$ multiplied by a constant stellar mass-to-light ratio Υ_*, describes the distribution of stellar mass in the galaxy. To mimick gradients of stellar mass-to-light ratio, each Gaussian could be assigned its own $\Upsilon_{*,i}$. To add a Navarro-Frenck-White (NFW) [TO DO: REF] dark matter halo component, a MGE generated from a fit to a NFW profile can be added to the stellar component. [TO DO: continue on p. 74]

Data comparison. As data we use stellar line-of-sight rotation velocities $v_{\mathrm{rot}} \equiv \langle v_{\mathrm{los}} \rangle$ [TO DO: consistent, los or rot] and velocity dispersions σ as described in §3. The JAM models give us a prediction for the second line-of-sight velocity moment v_{los}. The root mean square (rms) line-of-sight velocity v_{rms} allows a data-model comparison by relating theses velocities according to

$$v_{\mathrm{rms}}^2 = \langle v_{\mathrm{los}}^2 \rangle = v_{\mathrm{rot}}^2 + \sigma^2.$$

The model in Eq. [TO DO] predicts the intrinsic $\langle v_{\mathrm{los}}^2 \rangle$ at a given position on the sky, which have then to be modified to model the mode of observation, to be comparable to the measurements. The measured v_{rms} is a light-weighted mean for a pixel along the long-slit of the spectrograph, with height $L_y = 1$ arcsec [TO DO: REF: Dutton 2013] and a certain given extent in along the major axis, L_x, i.e. for a rectangular aperture

$$\mathrm{AP}(x,y) = \begin{cases} 1 & \text{for } -\frac{L_x}{2} \leqslant x \leqslant +\frac{L_x}{2} \text{ and } -\frac{L_y}{2} \leqslant y \leqslant +\frac{L_y}{2} \\ 0 & \text{otherwise} \end{cases} .$$

The light arriving at the spectrograph itself was subject to seeing, i.e. a Gaussian

$$\mathrm{PSF}(x,y) = \mathscr{N}(0, FWHM/2\sqrt{2\ln 2})$$

with FWHM=1.1 arcsec [TO DO: REF: Dutton 2013]. The model predictions have therefore to be convolved with the convolution kernel

$$\begin{aligned} K(x,y) &= (\mathrm{PSF} * \mathrm{AP})(x,y) \\ &= \frac{1}{4}\prod_{u\in\{x,y\}}\left[\mathrm{erf}\left(\frac{L_u/2-u}{\sqrt{2}\sigma_{\mathrm{seeing}}}\right) + \mathrm{erf}\left(\frac{L_u/2+u}{\sqrt{2}\sigma_{\mathrm{seeing}}}\right)\right] \end{aligned}$$

and weighted by the surface brightness $I(x, y)$ [TO DO: primed x and y or not????]

$$\begin{aligned} I_{\mathrm{obs}} &= I * K \\ \langle v_{\mathrm{los}}^2 \rangle|_{\mathrm{obs}} &= \frac{(I\langle v_{\mathrm{los}}^2 \rangle) * K}{I_{\mathrm{obs}}}. \end{aligned}$$

If provided with with the convolution kernel, the JAM code by [TO DO: REF: Cappellari 2008] [TO DO: reference code] performs the convolution numerically. We set $L_x = 0.21$ arcsec as the width of the model pixel, and get a prediction for the actual measurements in bins of width 0.63, 1.26 and 1.89 arcsec [TO DO: REF: Dutton 2013] as light-weighted mean from each 3, 6 and 9 model pixels.

3 DATA

[TO DO]

- Hubble Space teleskope (HST) imaging by Treu et al. (2011) in two filters (F450W amd F814W)
- I filter: for surface brightness distribution of J1331's bulge for Jeans modelling
- ??? filter: to identify bluish lensing images
- drizzled image

Stellar Kinematics. We use the stellar kinematics for J1331 measured by [TO DO: REF: Dutton 2013]. They obtained long-slit spectra along J1331's major-axis with the Low Resolution Imaging Spectrograph (LRIS) on the Keck I 10m telescope. The width of the slot was 1 arcsec and the seeing Conditions had a FWHM of ~ 1.1 arcsec. Spectra for spatial bins of different widths along the major axis were extracted. Analogously to [TO DO: REF: Dutton 2011] they measured line-of-sight rotation velocities ($v_{\rm rot}$) and stellar velocity dispersion (σ) by fitting Gaussian line profiles to emission lines in these spectra. Gas kinematics were extracted from fits to Hα and NII lines, as tracers for inonized gas.
The stellar kinematics, $v_{\rm rot}$, σ and $v_{\rm rms}^2 = v_{\rm rot}^2 + \sigma^2$ are shown in Figure 1d. The rotation curve reveals a counter-rotating core within 2 arcsec $\simeq 4$ kpc. Outside of $\sim 3.5 arcsec$ there is a steep drop in the dispersion, which is exptected at the boundary between the pressure supported bulge and the rotationally supported disk, which appears around this radius in the F450W filter in Figure 1a. However, in the brighter F814W filter in Figure 1b the large reddish bulge extends out to $\sim$5 arcsec.
Inside of ~ 4 arcsec, the data appears to be symmetric, outside of this the assumption of axisymmetry seems not to be valid anymore, considering the data. We add -2.3 km/s to the $v_{\rm rot}$ to ensure $v_{\rm rot}(R=0) \sim 0$ as a possible correction term for a systematic misjudgement of the systemic velocity. We also symmetrize the data within 4 arcsec and asign a minimum error of $\delta v_{\rm rms} > 5$ km/s to the $v_{\rm rms}$ data. In the JAM modelling, which is based on the assumption of axisymmetry, only kinematics within ~ 2.5 and 4 arcsec are used. Another reason to restrict to modelling on the bulge region is that our MGE in Table 2 is only a good representation of J1331's F814W light distribution inside ~ 5 arcsec.

4 RESULTS

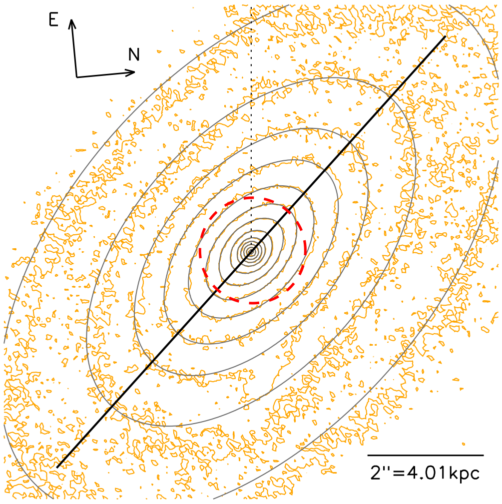

Figure 2. MGE for J1331's inner regions: Comparison of contours with constant F814W surface brightness of J1331's central region (orange lines) with the corresponding iso-brightness contours of the best fit MGE in table 2, convolved with the PSF in table 2, (gray lines). The MGE model is a good representation of the galaxy's light distribution within $\sim$ 5 arcsec. Image scaling and orientation are indicated in the figure. The black line has a length of 10 arcsec and it's orientation corresponds to the galaxy's position angle as found in table 3. For comparison the Einstein radius as found in table ??? is indicated as red dashed line. This MGE is used in the dynamical Jeans modelling in §???. [TO DO: explain how this MGE is used in dynamical modelling]

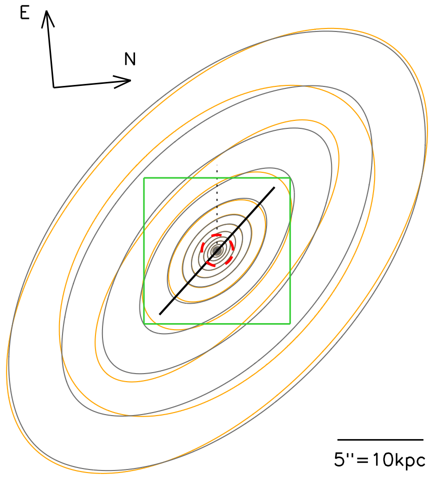

Figure 3. MGE for J1331's outer regions: Comparison of contours with constant surface brightness of the smooth IRAF ELLIPSE model for J1331 in the F814W filter (yellow) with a corresponding best fit MGE (gray lines). The green box corresponds to the image section shown in Fig. 2, with the Einstein radius as dashed red line. [TO DO: caption]

Table 1. F814W PSF MGE: Parameters of the circular four-Gaussian MGE in Eq. (3 fitted to the radial profile of the synthetic HST/F814W PSF image by [TO DO].

k	G_k	δ_k [arcsec]
1	0.184	0.038
2	0.485	0.085
3	0.222	0.169
4	0.109	0.487

4.1 Surface Photometry for J1331 with MGEs

In §??? we derived a mass model for J1331 from Lensing. In this section set up a model for the galaxy's intrinsic light distribution in terms of an MGE, which we will then compare to the mass distribution. The light model will also be the basis of the dynamical Jeans modelling in §???.
To derive J1331's surface brightness distribution, we use the HST image in the infrared F814W filter, shown in Fig. 1b. In infrared J1331's central old and smooth stellar component is more extended than in the F450W filter in Fig. 1a, which is more sensitive to young clumpy star-forming regions. In infrared the bulge is also much brighter than the bluish lens images and the imaging is less prone to extinction. The F814W image is therefore best suited for fitting a MGE.

PSF for the HST/F814W filter. We find a radial profile for the HST/F814W filter PSF from circular annuli within a synthetic PSF image from [TO DO: Where did we get this image from???], ignoring diffraction spikes. The one-dimensional MGE fit of Eq. (3) to this radial profile is performed using the code by [TO DO: REF and footnote to code]. The MGE parameters of the normalized PSF model are given in Tab. 1.

MGE for the inner regions. We fit a MGE to the smooth central region within radius $\sim$ 5 arcsec of the HST/WFPC2/WF3/F814W image of J1331 in Fig. 1b. Bright objects close to the galaxy, blobs possibly belonging to the background galaxy and parts of the foreground spiral arm were masked during the fit. J1331's galaxy center, position angle and average apparent ellipticity (see table 3) are found from the images weighted first and second moment. The MGE fit, as performed by the code Cappellari (2002), splits the image in annuli with the given ellipticity and position angle and sectors of 5° width and fits an 5-Gaussian MGE of the form in Eq. (1) convolved with the PSF MGE in table 1 to it. The best fit MGE (PSF convolved) is compared to the data in Fig. 2 and the corresponding parameters of the intrinsic surface brightness distribution are given in table 2. The fit is a very good representation of the light distribution in the inner 5 arcsec, but underestimates the light distribution outside of this.

MGE for the outer regions. To get an handle on the light distribution also in the outer parts of J1331, where spiral arms dominate, we first fit a IRAF ELLIPSE [TO DO: How to reference???] model to the F814W image (masking the brightest blobs in the spiral arms and outer regions). Only then we fit a 7-Gaussian MGE to the smooth ellipse model. The MGE does not perfectly reproduce the flattness of the ellipse model at every radius, but considering the spiral arm dominated outer regions of J1331, it is good enough for an approximate handling of the overall light distribution.

Table 2. J1331's F814W MGE: Parameters of the best fit MGE to the F814W surface brightness of J1331 in Fig. 1b. The fit is best inside an radius of 5 arcsec. The galaxy center and position angle, which gives the orientation of the MGE with respect to the original image, are given in table 3. This MGE is used in the dynamical modelling in §???. The first column gives the total F814W luminosity of the Gaussian in Eq. (2) in units of counts. The second column is the corresponding I-band peak surface brightness in Eq. (1) in units of a luminosity surface density, calculated from the first column following the procedure described in §???. The third and fourth column give the dispersion and the last column the axis ratio of the Gaussian in Eq. (1).

k	total luminosity L_k [counts]	surface density $I_{0,k}$ $[L_\odot/\mathrm{pc}^2]$	Gaussian dispersion σ_k [arcsec]	σ_k [kpc]	axis ratio q'_k
1	9425.96	20768.	0.051	0.103	1.00
2	13173.0	3161.2	0.178	0.358	0.76
3	40235.0	1588.2	0.503	1.008	0.58
4	67755.2	502.25	1.180	2.368	0.56
5	203677.	136.51	3.891	7.805	0.57

Table 3. Galaxy Parameters of J1331

redshift	z_d	0.113	(Brewer et al. 2012)
angular diameter distance	D_d [Mpc]	414	
scaling	1 kpc / 1 arcsec	2.006	
position angle	ϕ [degrees]	wrt what???	
average axis ratio	q'	0.598	
average ellipticity	$\epsilon = 1 - q'$	0.402	
apparent I-band magnitude	m_I [mag]	15.77	
total I-band luminosity	$L_\mathrm{tot,I}$ $[10^{10} L_\odot]$	5.6	
effective half-light radius	R_eff [arcsec]	2.6	
	R_eff [pc]	5.2	

Transformation into physical units. To transform the MGE in units of counts into physical units, we apply a simplified version of the procedure described in Holtzman et al. (1995), analogous to [TO DO: Cappellari Read me file???] The scaling of the drizzled HST/WFC3 images is $S = 0.05$ arcsec/pixel and the total exposure time $T = 1600$ sec. The total F814W luminosity in counts of each Gaussian of the MGE has a central surface brightness in counts per pixel of

$$C_0[\text{counts/pixel}] = \frac{L[\text{counts}]}{2\pi\sigma[\text{pixel}]^2 q}.$$

This is then transformed into an I-band surface brightness via

$$\mu_I \simeq -2.5\log_{10}\left(\frac{C_0[\text{counts/pixel}]}{T[\text{sec}]\cdot S[\text{arcsec/pixel}]^2}\right) + Z + C + A_I, \quad (11)$$

where $Z \simeq 21.62$ is a the zero-point from Holtzman et al. (1995) (updated according to Dolphin (2000, 2008)) for the photometric system of the HST/WFPC2 camera and the F814W filter plus a correction for the difference in gain between calibration and observation. $C = 0.1$ corrects for the finite aperture of the WFPC2. And $A_I = 0.015$ mag is the extinction in the I-band tpwards J1331, according to the NASA/IPAC Extragalactic Database [TO DO: proper reference]. The color-dependent correction between the F814W filter and the I-band of the UBVRI photometric system is small (Holtzman et al. 1995) and we neglect it therefore. The last step is to transform the surface brightness μ_i in mag to the I-band surface density of the Gaussian in $L_\odot/\mathrm{pc}^2$ as

$$I_0[L_\odot \mathrm{pc}^{-2}] = (64800/\pi)^2\,(1+z)^4\,10^{0.4\left(M_{\odot,I}-\mu_I\right)},$$

where the term with z accounts for redshift dimming and $M_{\odot,I} = 4.08$ mag is the sun's absolute I-band magnitude (Binney & Merrifield 1998). The luminosity L_k[counts] and the corresponding surface brightness density $I \equiv I_{0,k}[L_\odot \mathrm{pc}^{-2}]$ of each Gaussian are given in Table 2. [TO DO: I'm really confused about this. Check, that everything is correct and the naming of quantities, e.g. with or without subscripts of 0, is fine???] [TO DO: Maybe shift to appendix???]

Inclination. To estimate the inclination of J1331 with respect to the observer, we use the observed axis ratio of the flattest ellipse in the Iraf Ellipse [TO DO] model for J1331, which is $q' = 0.42$. This is similar to the disk axis ratio of $q' = 0.40$ found by Treu et al. (2011) [TO DO: CHECK]. If a typical thickness of an oblate disk was around $q_0 \sim 0.2$ [TO DO: REF: Holmberg 1985], the inclination would follow from $\cos^2 i = \frac{q'^2 - q_0^2}{1-q_0^2}$ and a correction of $+3°$ [TO DO: REF: Tully 1988]. Our estimate for the inclination is therefore $i \approx 70°$.

Total luminosity and effective radius. J1331's total I-band luminosity is easily determined by summing up the luminosity contributions of all the Gaussians of the MGE for the outer regions (shown as gray lines in Fig. 3). We find $L_\mathrm{tot,I} \simeq 5.6 \cdot 10^{10} L_\odot$. This corresponds to an apparent magnitude of $m_I = 15.77$ mag. We determine the circularized effective radius R_eff of J1331 from the definition $L(< R_\mathrm{eff}) \equiv \frac{1}{2} L_\mathrm{tot}$ and the growth curve $L(< R)$ from the MGE model of the outer regions [TO DO: Maybe I need a table anyway???], where R is the projected radius on the sky [TO DO: Or is it R'???]. We find the effective radius to be $R_{\rm eff} \simeq 2.6$arcsec$\hat{=}$5.2kpc. All values are summarized in Table 3.

[TO DO: Stuff to mention]

- the deporjecten if the galaxy under the assumption of oblate axisymmetry and an estimated inclination of $\sim 70^\circ$ can be performed analytically.

	A	B	C	D	G
x_i [pixel]	12.1	-8.5	21.7	-3.3	$0.5 \pm\sqrt{2}$
y_i [pixel]	16.6	-10.4	-0.5	19.2	$0.5 \pm\sqrt{2}$

Table 4. Positions of the lensing images (A-D) and the galaxy center (G) in fig. 1c. The image positions were determined from the lens subtracted image for J1331 in figure 4 of Brewer et al. (2012), rotated to the (x, y) coordinate system in fig. 1c. The pixel scale is 1 pixel = 0.05 arcsec and the error of each image position is ± 1 pixel. *SMALL PROBLEM: Somehow I used $\sqrt(2)$ pixel as the error on the galaxy center in the Monte Carlo sampling code instead of the 0.5 pixel I claim here. Should I change this table and the error bars in the figures to match this bug????*

4.2 Mass distribution from Lensing

Image Positions. We determine the positions of the lensing images by first subtracting a smooth model for the galaxy's surface brightness from the original image. As models we use MGE fits (cf. §**??**) and IRAF ellipse fits (???) to the galaxy in each the F450W and F814W filter. (For example the MGE we use for F814W is the MGE given in tab. 2 convolved with the PSF in tab. 1.) The lensing images become then visible in the residuals (see fig. 1c). Because the lensing images are extended, we use the position of the brightest pixel in each of the images. We also use the F814W-MGE subtracted residuals from Brewer et al. (2012). The lensing positions as determined from the latter are given in tab. 4. The scatter of lensing positions as determined from subtracting different surface brightness models from the galaxy in different filters gives an error of ±1 pixel on the image positions.

Best fit lens model. The best fit lens model for the image positions in tab. 4 is given in the first column of tab. 5. Fig. 4a shows the corresponding critical curve, caustic and Einstein radius, and the best fit source position. In this case, where $\alpha = 1$, the critical curve is also an equidensity contour of the galaxy model. Fig. 4b overplots the smoothed residuals from the F814W image subtracted by the IRAF ellipse fit to the surface brightness with the contours of the best fit model's time delay surface. This demonstrates that, although we did not include any information about the shape of the lensing images in the fit, it is consistent with the predicted distortion for an extended source by the best fit lens model.
To estimate how the uncertainties in the determination of the image positions and galaxy center affect the results, we Monte Carlo sample random positions from a two-dimensional Normal distribution centered at the positions in tab. 4 and a standard deviation corresponding to the measurement error of 1 pixel. A Gaussian fit to the resulting distributions of best fit values leads to the constraints on the shape parameters and Einstein quantities in the second column in tab. 5. We therefore constrain the Einstein radius to within 2%, $R_{\text{ein}} = (0.91 \pm 0.02)$ arcsec and the projected mass within the critical curve with a relative error of 4%, $M_{\text{crit}} = (7.9 \pm 0.3) \cdot 10^{10} M_\odot$. Our measurement of R_{ein} is consistent with that from Brewer et al. (2012), $R_{\text{ein,SWELLS}} = (0.96 \pm 0.04)$ arcsec. The relative difference between our critical mass and that of Brewer et al. (2012), $M_{\text{crit,SWELLS}} = (8.86 \pm 0.61) \cdot 10^{10} M_\odot$, is 13%.

Table 6. ???

Total I-band luminosity within R_{ein} $L_{\text{I,ein}}$ $[10^{10} L_\odot]$	Mass-to-light ratio within R_{ein} $\Upsilon_{\text{I,ein}} = M_{\text{ein}}/L_{\text{I,ein}}$ $[\Upsilon_\odot]$
1.40	5.56

Comparison with Light Distribution. Fig. 5b shows the surface mass distribution as predicted by the best fit model in tab. 5. We introduce random noise according to the uncertainties in the Fourier shape parameters to create a mock observation that visualizes the effect of the measurement errors. From the mock image's second moment we find an average axis ratio for the lens mass model of $q_{\text{lens}} \simeq 0.695$, which is consistent with the one found by Brewer et al. (2012), $q_{\text{lens,SWELLSIII}} = 0.67 \pm 0.09$, while the light's average axis ratio in Table 3 is $q' = 0.598$.
To be able to compare the predicted mass distribution to the observed light distribution, we transform the surface brightness into a mass density: We first integrate the MGE in tab. 2 to get the total luminosity within the Einstein radius and the predicted mass-to-light ratio as $\Upsilon_{\text{I,ein}} = M_{\text{ein}}/L_{\text{I,ein}}$. Fig. 5a shows then the observed surface brightness in the F814W filter multiplied by $\Upsilon_{\text{I,ein}}$. Fig. 5c finally compares equidensity contours at the same values of both the predicted lens mass distribution and the observed surface brightness times $\Upsilon_{\text{I,ein}}$.
Figure 5 leads to the following three findings: 1.The mass predicted from lensing and the observed light distribution are oriented in the same direction. 2. Within the Einstein radius, mass and light distribution have the same shape, while further out the mass distribution is more roundish. 3. The light distribution drops faster than the mass with increasing radius.
Reasons for the difference in observed light and measured mass distribution could be, e.g. an apparent change of shape due to dust extinction, a strongly changing Υ_*, or the stellar component of the galaxy could be superimposed by a more roundish dark matter component.

[TO DO: Stuff to mention]

- best fit lens total mass distribution of J1331 has the same position angle and a similar elliptical shape as the surfache brightness distributon, but is slightly rounder, and could be consistent with a flat rotation curve.

Table 5. ??? in tab. 4, for $\alpha = 1$

		lens model for peak image positions	lens model from Monte Carlo sampling of image positions			
Einstein Radius	$R_{\rm ein}$ [arcsec]	0.907	0.91	$\pm$	0.02	(2%)
Einstein Mass	$M_{\rm ein}$ [$10^{10} M_{\odot}$]	7.72	7.8	$\pm$	0.3	(4%)
Critical Mass	$M_{\rm crit}$ [$10^{10} M_{\odot}$]	7.87	7.9	$\pm$	0.3	(4%)
Source Position	ξ [arcsec]	0.095	0.09	$\pm$	0.03	(28%)
	η [arcsec]	0.107	0.10	$\pm$	0.03	(27%)
Fourier Coefficients	a_0	1.814	1.82	$\pm$	0.04	(2%)
	a_2	0.012	0.011	$\pm$	0.004	(35%)
	b_2	-0.057	-0.06	$\pm$	0.01	(25%)
	a_3	-0.0001	0.0000	$\pm$	0.0006	
	b_3	-0.0002	0.000	$\pm$	0.001	

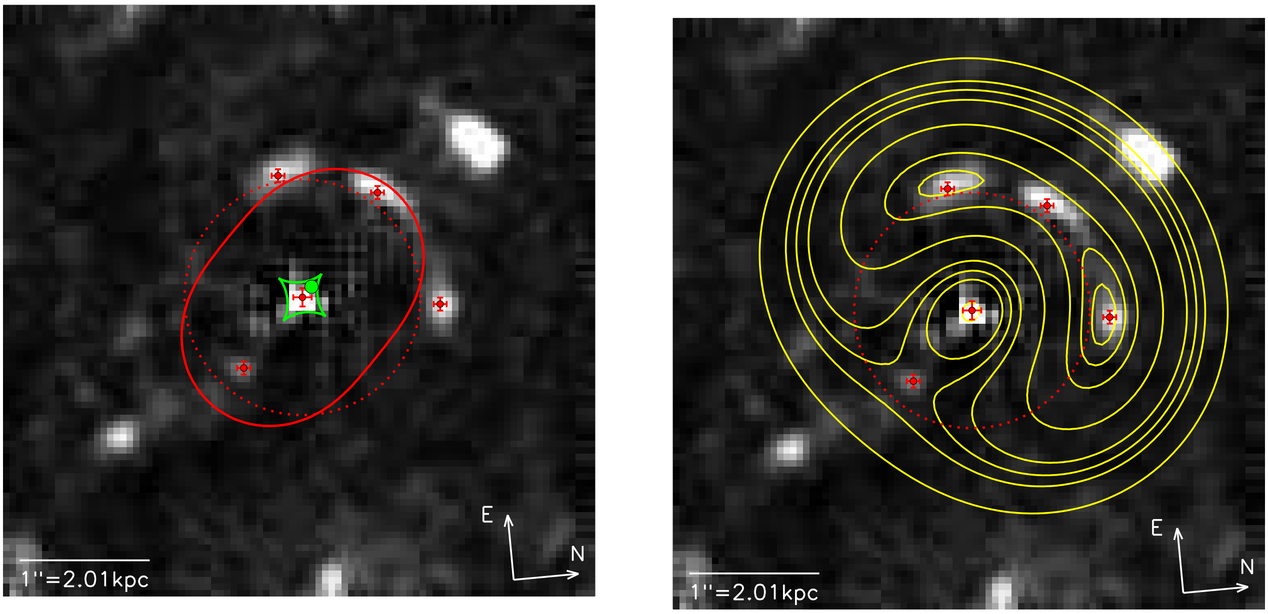

(a) ??? Critical curves, Einstein radius, caustics, source position for best fit model. ??? [TO DO: nice caption]

(b) ??? Time delay surface ??? [TO DO: nice caption]

Figure 4. ???

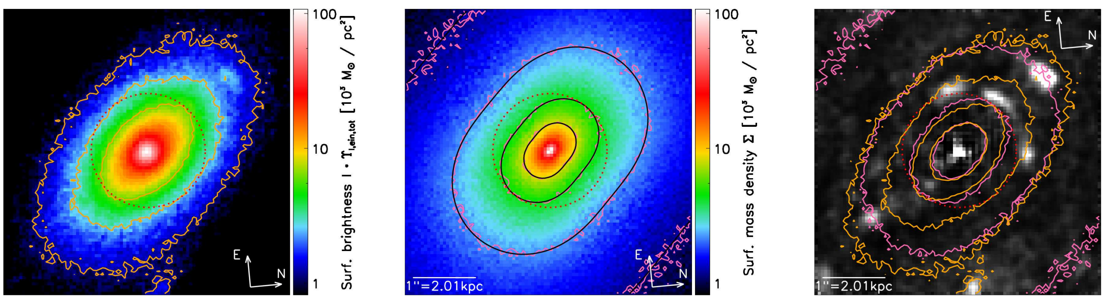

(a) ???

(b) ???

(c) ???

Figure 5. ??? Preliminary crappy caption: Left: OBSERVED surface bightness multiplied with M/L in Einstein radius (overplotted in red). Middle: BEST FIT MODEL for mass distribution from lensing (including "wriggles" due to uncertainties in image positions). Contours are at the same levels. Right: Same contours, to directly show the difference in shape. ??? [TO DO: nice caption]

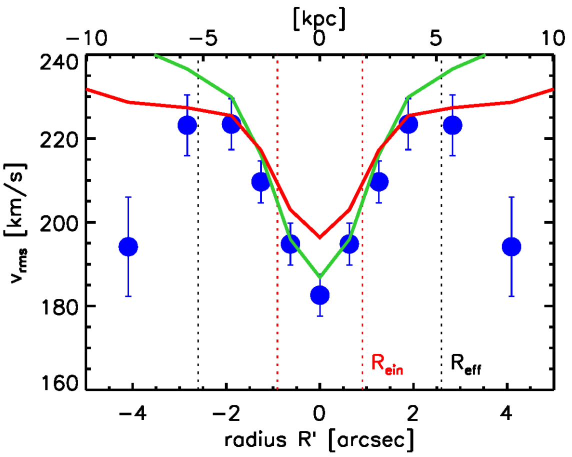

Figure 6. Comparison (not a fit!) of the symmetrized stellar $v_{\rm rms}$ data of J1331 (blue dots) with JAM models generated from mass distributions which were independently derived from lensing constraints in §4.2. The red solid line corresponds to the lens model for a flat rotation curve ($\alpha = 1$) in Table 5; the green line is a best fit lens model found analogously from the image positions, but for a fixed rotation curve slope of $\alpha = 1.1$. For the JAM modelling a best fit MGE to the lens mass models were used, as well as the observed surface brightness MGE in Table 2, assuming velocity isotropy $\beta_z = 0$ and an inclination of $i = 70°$.The red and black dotted lines are the Einstein radius and the effective half-light radius, respectively.

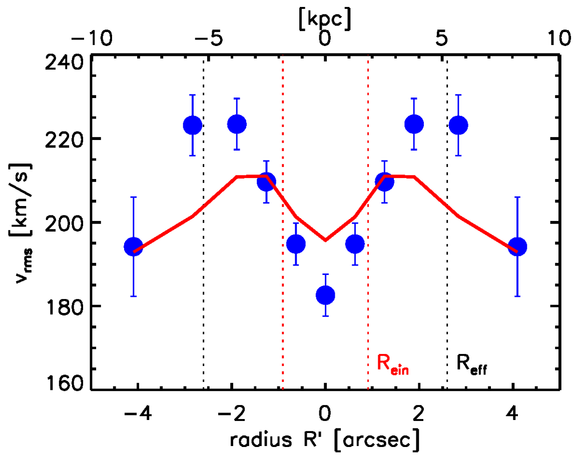

Figure 7. Comparison of the symmetrized $v_{\rm rms}$ data of J1331 (blue dots) with a best fit dynamical JAM model (solid red line) assuming mass-follows-light and with two free parameters: $\Upsilon_{I,\rm tot}^{\rm dyn}$, the total I-band mass-to-light ratio found from dynamics, which converts the observed surface brightness in Table 2 into a mass distribution, and the velocity anisotropy parameter β_z. The "best" fit is $\Upsilon_{I,*}^{\rm dyn} = 4.8 \pm 0.1$ and $\beta_z = -0.5$, where the latter is however pegged at the lower limit of the allowed value range. This is obviously not a good model.

4.3 JAM based on Surface Brightness

... with the Lens Mass Model. Our first JAM model uses the mass distribution which we found from lensing constraints in §4.2 to generate an independent prediction for the $v_{\rm rms}$ curve following the procedure in §2.3. In addition to the flat rotation curve model with $\alpha = 1$ in Table 5, we also investigate a lens model, which was found as a best fit to the lensing images when assuming a [TO DO: rising or droppint???] rotation curve slope of $\alpha = 1.1$. The predictions are compared with the data in Figure 6. The agreement between the lensing prediction and the observed kinematics within $R' \sim 3$ arcsec is striking, especially around the Einstein radius. The $\alpha = 1$ model fits the wings nicely, while the $\alpha = 1.1$ model recreates almost exactly the observed central dip. The sharp drop in $v_{\rm rms}$ around $R' \sim 3$ arcsec [TO DO: make sure all projected Rs are R'] cannot be reproduced, however. But outside of the Einstein radius our lensing models are only extrapolations and the true constraint is around the Einstein radius.

... with "Mass-follows-Light" and Velocity Anisotropy. Our second JAM model is a mass-follows-light model, which are often used in dynamical JAM modelling (e.g. van de Ven et al. (2010); Cappellari et al. (2006)), where the mass distribution ins generated by multiplying the light distribution in Table 2 by a constant total mass-to-light ratio $\Upsilon_{I,\rm tot}^{\rm dyn}$. This assumes that the dark matter is always a constant fraction of the total matter distribution everywhere. This simplified model sometimes gives good representations of the inner parts of galaxies, where the stellar component dominates. In addition to the free fit parameter $\Upsilon_{I,\rm tot}^{\rm dyn}$, we also allow for a overall constant but non-zero velocity anisotropy β_z. The best fit is found by minimizing χ^2 between the $v_{\rm rms}$ data and model prediction and is demonstrated in Figure 7. For β_z we impose the fitting limits $\beta_z \in [-0.5, +0.5]$. While the outer parts of galaxies often show radially biased velocity anisotropy up to ~ 0.5 (from dynamical modelling of observed elliptical galaxies (e.g. Kronawitter et al. (2000)) and cosmological simulations (e.g. Diemand et al. (2004); Fukushige & Makino (2001)), the centers of galaxies are near-isotropic or have negative velocity anisotropy (Gebhardt et al. 2003). Only in extreme models (e.g. around in-spiralling supermassive black holes (Quinlan & Hernquist 1997)) velocity anisotropies as low as ~ -1 have been found. A lower limit of $\beta_z \geqslant -0.5$ is a realistic assumption for J1331, for which we do not expect extreme dynamical conditions. The best fit in Figure 7 however strives to very negative velocity anisotropies to be able to get the deep central dip in the $v_{\rm rms}$ curve. But $\beta_z = -0.5$ is not even a remotely agreeable fit and lower anisotropies are not to be expected and realistic. We also tested radial profiles for $\beta_z(R)$ of the form proposed by Baes & van Hese (2007), which was however equally unable to reproduce the data. We conclude, that this is due to the well-known degeneracy between anisotropy and mass profile [TO DO: REF] and the mass-follows-light model is *not* a good representation of the mass distribution in J1331's inner regions.

... with Increasing Mass-to-Light Ratio. In §4.2 we found from the lensing, that the light distribution might drop faster with radius than the mass distribution. This would correspond to a radially increasing total mass-to-light ratio. As velocity anisotropy alone cannot explain the observed kinematics in a simple a mass-follows-light model, we now allow for an mass-to-light ratio gradient in the JAM modelling to generate a mass model from the light distribution in Table 2. We do this by assigning each of the five

Gaussians in the MGE its own mass-to-light ratio and replace the total luminosity in Eq. (2) L_i with the Gaussians total Mass $M_i = \Upsilon_i L_i$. We treat the five Υ_i as free parameters and only require that $\Upsilon_j \geqslant \Upsilon_i$ when the corresponding $\sigma_j \geqslant \sigma_i$ to ensure an overall mass-to-light ratio that is increasing with radius. [TO DO: Discuss Figure]

[TO DO]

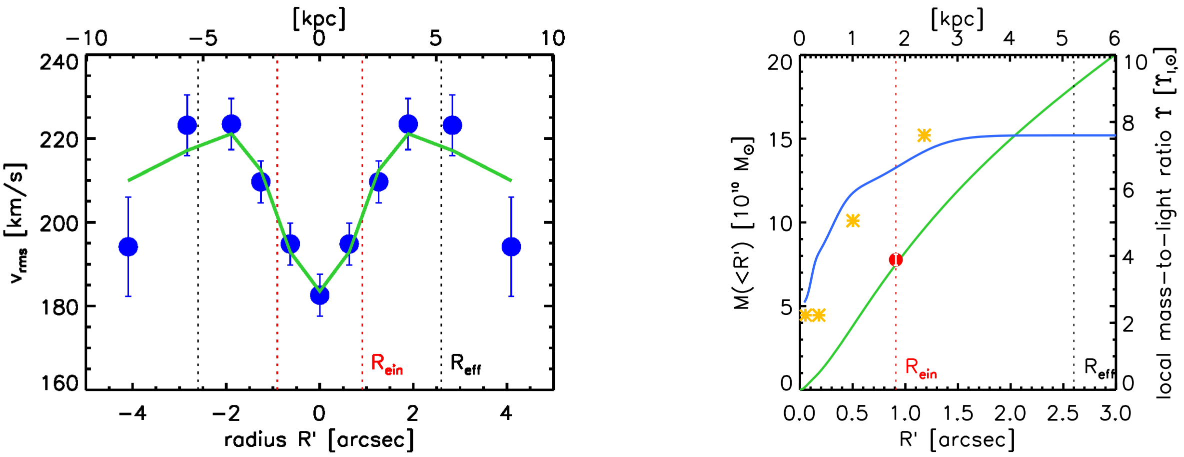

(a) Comparison between the stellar $v_{\rm rms}$ data (blue points) and the best fit JAM model using an increasing

(b) ??? [TO DO: Make figure wider. Include legend.???] [TO DO: Why does this plot look different than the others???]

Figure 8. JAM model found by using an increasing mass-to-light ratio to generate a mass model from the light distribution in Table 2. [TO DO]??? Using the surface brightness MGE for the dynamical modelling: each Gaussian got it's own M/L such that the overall M/L is increasing with radius. This is the best fit model. The enclosed mass is overplotted with Einstein mass with 4% error (overplotted, not fitted). ??? [TO DO: nice caption]

4.4 JAM with a NFW Dark Matter Halo

Sampling with a Markov Monte Carlo Chain

[TO DO]

Predicting the Rotation Curve at larger Radii

[TO DO]

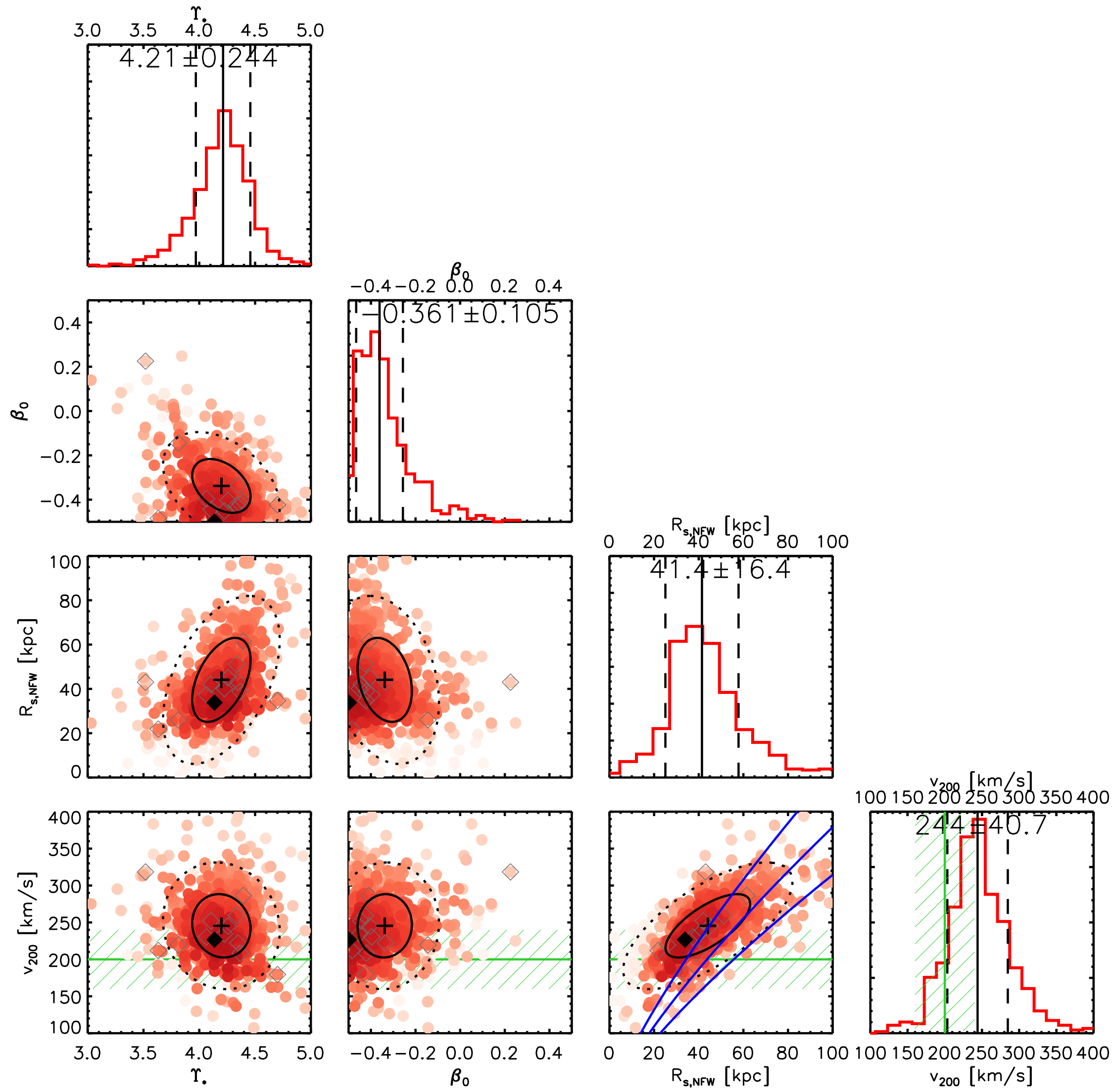

Figure 9. ??? Preliminary crappy caption: Result of the MCMC sampling of the parameter space for a model with NFW halo and constant velocity anisotropy. Green and blue shows the priors. Grey diamonds are the models shown in next figure. ??? [TO DO: nice caption]

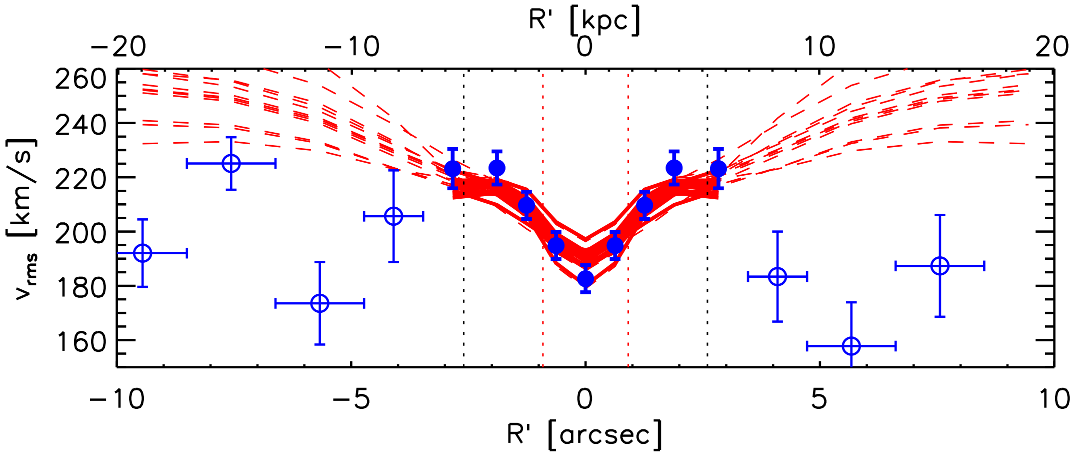

(a) ???

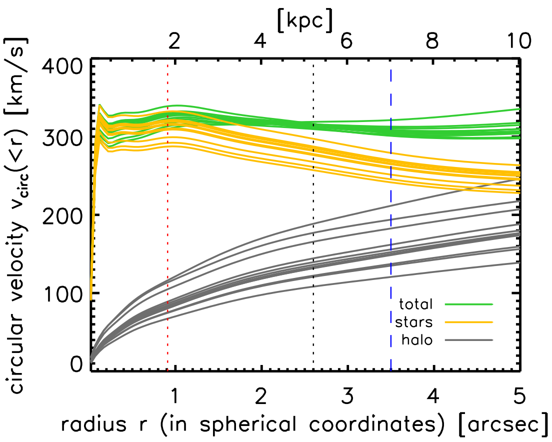

(b) ????????

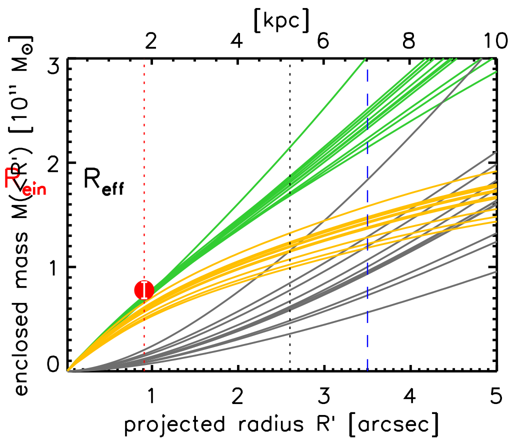

(c) ???

Figure 10. ??? Preliminary crappy caption: 12 samples from the parameter pdf found with the MCMC above for the model with NFW halo and constant velocity anisotropy. Big red dot shows the Einstein mass with a 10% error (used in fit). ??? [TO DO: nice caption]

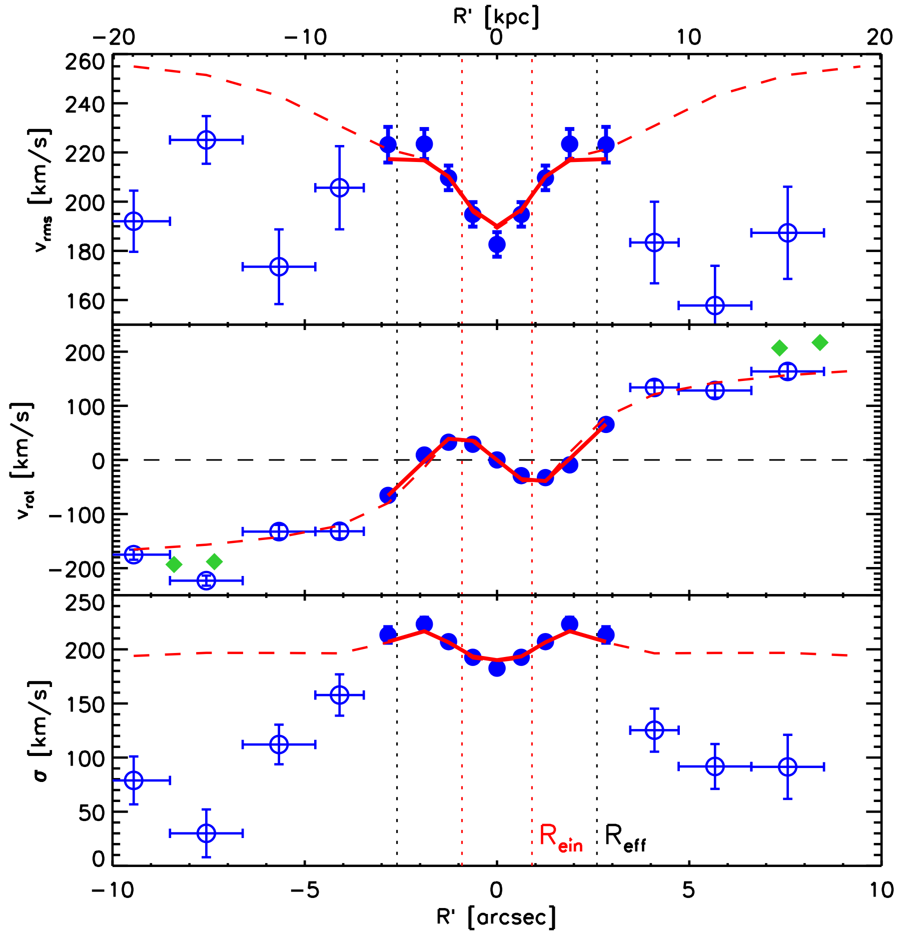

Figure 11. ??? Preliminary crappy caption: Model: NFW halo and constant velocity anisotropy, using the the mean / peak values of the MCMC result in the above pdf for the model parameters. Fitting one more free parameter to the rotation curve in the inner regions, predicting the rotation curve and dispersion at larger radii. Green dots are gas kinematics. ??? [TO DO: nice caption]

5 DISCUSSION AND CONCLUSION

5.1 Stellar mass-to-light ratios

[TO DO] [TO DO: Also compare with results from Treu et al.]

Collection of thoughts

art on page 62

5.2 Does J1331 have a Merger History?

[TO DO]

5.3 Summary

[TO DO]

REFERENCES

Baes M., van Hese E., 2007, Astronomy and Astrophysics, 471, 419
Bendinelli O., 1991, Astrophysical Journal, 366, 599
Binney J., Merrifield M., 1998, Galactic Astronomy
Brewer B. J., Dutton A. A., Treu T., Auger M. W., Marshall P. J., Barnabè M., Bolton A. S., Koo D. C., Koopmans L. V. E., 2012, Monthly Notices of the RAS, 422, 3574
Cappellari M., 2002, Monthly Notices of the RAS, 333, 400
Cappellari M., 2008, Monthly Notices of the RAS, 390, 71
Cappellari M., Bacon R., Bureau M., Damen M. C., Davies R. L., de Zeeuw P. T., Emsellem E., Falcón-Barroso J., Krajnović D., Kuntschner H., McDermid R. M., Peletier R. F., Sarzi M., van den Bosch R. C. E., van de Ven G., 2006, Monthly Notices of the RAS, 366, 1126
Diemand J., Moore B., Stadel J., 2004, Monthly Notices of the RAS, 352, 535
Dolphin A. E., 2000, Publications of the ASP, 112, 1397
Dolphin A. E., , 2008, Zero Points relative to Holtzman et al. (1995)
Dutton A. A., Treu T., Brewer B. J., Marshall P. J., Auger M. W., Barnabè M., Koo D. C., Bolton A. S., Koopmans L. V. E., 2013, Monthly Notices of the RAS, 428, 3183
Emsellem E., Dejonghe H., Bacon R., 1999, Nonthly Notices of the RAS, 303, 495
Emsellem E., Monnet G., Bacon R., 1994, Astronomy and Astrophysics, 285, 723
Evans N. W., Witt H. J., 2003, Monthly Notices of the RAS, 345, 1351
Fukushige T., Makino J., 2001, Astrophysical Journal, 557, 533
Gebhardt K., Richstone D., Tremaine S., Lauer T. R., Bender R., Bower G., Dressler A., Faber S. M., Filippenko A. V., Green R., Grillmair C., Ho L. C., Kormendy J., Magorrian J., Pinkney J., 2003, Astrophysical Journal, 583, 92
Holtzman J. A., Burrows C. J., Casertano S., Hester J. J., Trauger J. T., Watson A. M., Worthey G., 1995, Publications of the ASP, 107, 1065
Kochanek C. S., 1991, Astrophysical Journal, 373, 354
Kronawitter A., Saglia R. P., Gerhard O., Bender R., 2000, Astronomy and Astrophysics, Supplement, 144, 53
Monnet G., Bacon R., Emsellem E., 1992, Astronomy and Astrophysics, 253, 366
Narayan R., Bartelmann M., 1999, in Dekel A., Ostriker J., eds, Formation of Structure in the Universe, Proceedings of the 1995 Jerusalem Winter School Lectures on Gravitational Lensing. Cambridge University Press, pp 360–432
Navarro J. F., Frenk C. S., White S. D. M., 1996, Astrophysical Journal, 462, 563
Oort J. H., 1932, Bulletin Astronomical Institute of the Netherlands, 6, 249
Quinlan G. D., Hernquist L., 1997, New Astronomy, 2, 533
Rubin V. C., Thonnard N., Ford Jr. W. K., 1978, Astrophysical Journal, Letters, 225, L107
Treu T., 2010, Annual Review of Astron and Astrophys, 48, 87
Treu T., Dutton A. A., Auger M. W., Marshall P. J., Bolton A. S., Brewer B. J., Koo D. C., Koopmans L. V. E., 2011, Monthly Notices of the RAS, 417, 1601
van de Ven G., Falcón-Barroso J., McDermid R. M., Cappellari M., Miller B. W., de Zeeuw P. T., 2010, Astrophysical Journal, 719, 1481
van den Bosch R. C. E., van de Ven G., Verolme E. K., Cappellari M., de Zeeuw P. T., 2008, Monthly Notices of the RAS, 385, 647